







High pressure synthesis of phosphine from the elements and the discovery of the missing $(\text{PH}_3)_2\text{H}_2$ tile

Matteo Ceppatelli ^{1,2}✉, Demetrio Scelta ^{1,2}, Manuel Serrano-Ruiz², Kamil Dziubek ^{1,2}, Gaston Garbarino ³, Jeroen Jacobs³, Mohamed Mezouar ³, Roberto Bini ^{1,2,4} & Maurizio Peruzzini²

High pressure reactivity of phosphorus and hydrogen is relevant to fundamental chemistry, energy conversion and storage, and materials science. Here we report the synthesis of $(\text{PH}_3)_2\text{H}_2$, a crystalline van der Waals (vdW) compound (*I4cm*) made of PH_3 and H_2 molecules, in a Diamond Anvil Cell by direct catalyst-free high pressure (1.2 GPa) and high temperature ($T \lesssim 1000$ K) chemical reaction of black phosphorus and liquid hydrogen, followed by room T compression above 3.5 GPa. Group 15 elements were previously not known to form H_2 -containing vdW compounds of their molecular hydrides. The observation of $(\text{PH}_3)_2\text{H}_2$, identified by synchrotron X-ray diffraction and vibrational spectroscopy (FTIR, Raman), therefore represents the discovery of a previously missing tile, specifically corresponding to P for pnictogens, in the ability of non-metallic elements to form such compounds. Significant chemical implications encompass reactivity of the elements under extreme conditions, with the observation of the P analogue of the Haber-Bosch reaction for N, fundamental bond theory, and predicted high pressure superconductivity in P-H systems.

¹LENS, European Laboratory for Non-linear Spectroscopy, Via N. Carrara 1, I-50019 Firenze, Sesto Fiorentino, Italy. ²ICCOM-CNR, Institute of Chemistry of OrganoMetallic Compounds, National Research Council of Italy, Via Madonna del Piano 10, I-50019 Firenze, Sesto Fiorentino, Italy. ³ESRF, European Synchrotron Radiation Facility, 71 Avenue des Martyrs, 38000 Grenoble, France. ⁴Dipartimento di Chimica "Ugo Schiff" dell'Università degli Studi di Firenze, Via della Lastruccia 3, I-50019 Firenze, Sesto Fiorentino, Italy. ✉email: matteo.ceppatelli@iccom.cnr.it

The history of the layered structures of phosphorus has been intimately related to pressure since 1914¹, when Percy Bridgman, who may be considered the founder of high pressure science, first synthesized black phosphorus (P_{black}), whose characteristic crystalline layered structure corresponds to the thermodynamically stable allotrope of the element². Rhombohedral A7, another layered structure of phosphorus, was later discovered by compression of P_{black} above 5 GPa³. Recently, a high pressure study, based on synchrotron X-ray diffraction (XRD) in Diamond Anvil Cell (DAC), has made another mark in the history of the layered structures of phosphorus, providing a clear insight about the mechanism of interlayer bond formation and significantly raising the pressure limit for the existence of the phosphorus layers up to ~ 30 GPa at room T^{4,5}.

In 2014, the advent of phosphorene⁶, a 2D corrugated monoatomic layer of phosphorus atoms with extraordinary properties, whose stacking actually builds up the the crystal structure of P_{black} has sharply raised the attention of the scientific community about the layered structures of element 15, with considerable experimental and theoretical efforts nowadays in attempting to stabilize and functionalize the phosphorus layers by the introduction of molecular fragments⁷ or atoms, like for example H⁸.

During the last two decades, the generation of pressure in the GPa range has greatly expanded the horizon of chemistry under extreme conditions⁹. In particular, the combination of pressure with high temperature or electronic photo-excitation has been shown to be a very effective and extremely powerful tool for opening selective reactive paths^{10,11}, activating chemical reactivity in notoriously non interacting systems at ambient conditions¹², like here P and H, and for synthesizing new unexpected compounds^{13,14}, thus suggesting the idea of investigating the so far unexplored chemistry of the phosphorus-hydrogen system under high pressure conditions.

Besides H-functionalization and stabilization of the layered structures of phosphorus, the direct chemical reactivity between elemental phosphorus and hydrogen under high pressure conditions is indeed currently of extreme interest for relevant issues essentially related to the chemistry and physics of phosphorus hydrides. Molecular hydrides of non-metallic elements have indeed always attracted the attention of high pressure chemists, physicists and materials scientists for their potential applications as superconducting¹⁵ and H-storage materials, due to their high H content and to the ability of forming stoichiometric van der Waals (vdW) compounds in the presence of H_2 ^{16,17}. Since the first report of a vdW solid made of He and N_2 ¹⁸, many H_2 -containing vdW compounds involving elements from group 14 to group 18, including nobles gases, simple diatomics and molecular hydrides of non-metallic elements, have been experimentally observed at high pressure: $CH_4(H_2)_4$ ¹⁹, CH_4H_2 ¹⁹, $(CH_4)_2H_2$ ¹⁹, $SiH_4(H_2)_2$ ²⁰, $GeH_4(H_2)_2$ ²¹, $N_2(H_2)_2$ ²², $(N_2)_6(H_2)_7$ ^{22,23}, $(O_2)_3(H_2)_4$ ²⁴, $(H_2O)_6H_2$ ²⁵, $(H_2O)H_2$ ²⁵, $(H_2S)_2H_2$ ²⁶, $(H_2Se)_2H_2$ ²⁷, $(HI)_2H_2$ ²⁸, $Ar(H_2)_2$ ²⁹, $Kr(H_2)_2$ ³⁰, $Xe(H_2)_8$ ^{31,32}. Nevertheless, among those formed by H_2 and by the molecular hydride of a non-metallic element reported so far, none involves any of group 15 elements³³. Within this picture, if the elements in the periodic table are to be considered tiles arranged on the basis of their electronic configuration, which determines their properties, then group 15 elements, named pnictogens, represent the missing tiles in this arrangement.

Phosphorus is here of particular relevance. Indeed the recent discovery of high superconducting T_c of 203 K in H_2S at high pressure³⁴, in agreement with the Bardeen-Cooper-Schrieffer (BCS) phonon mediated theory of high temperature superconductivity³⁵, has further promoted the search for a similar behavior in the hydrides of neighbor elements in the periodic table. In particular, in the case of phosphorus the report of high pressure

superconductivity in phosphine ($T_c > 100$ K, $P > 200$ GPa)³⁶, has stimulated several theoretical studies aimed at exploring the structure and stability of PH_3 at high pressure and the substantially unknown high pressure behavior of the phosphorus-hydrogen system, with the prediction of superconducting layered structures formed by these two elements above 80 GPa^{37–39}.

Finally, the formation, stability and decomposition of PH_3 in presence of H_2 are relevant astrochemical issues⁴⁰ related to the composition of giant planets, such as Jupiter and Saturn^{41,42}, and their moons⁴³, where PH_3 and H_2 have been detected.

Within this picture, in this paper we report a synchrotron XRD and vibrational spectroscopy (FTIR and Raman) study of the high pressure chemistry occurring between black phosphorus and molecular hydrogen at pressure of 1.2–1.5 GPa and temperature $\lesssim 1000$ K, where phosphorus is in the layered crystalline orthorhombic structure (A17), commonly known as black phosphorus, and H_2 is liquid⁴⁴ (Fig. 1). In these thermodynamic conditions PH_3 is directly synthesized from the elements. On further room T compression, between 3.5 and 4.1 GPa, PH_3 combined with

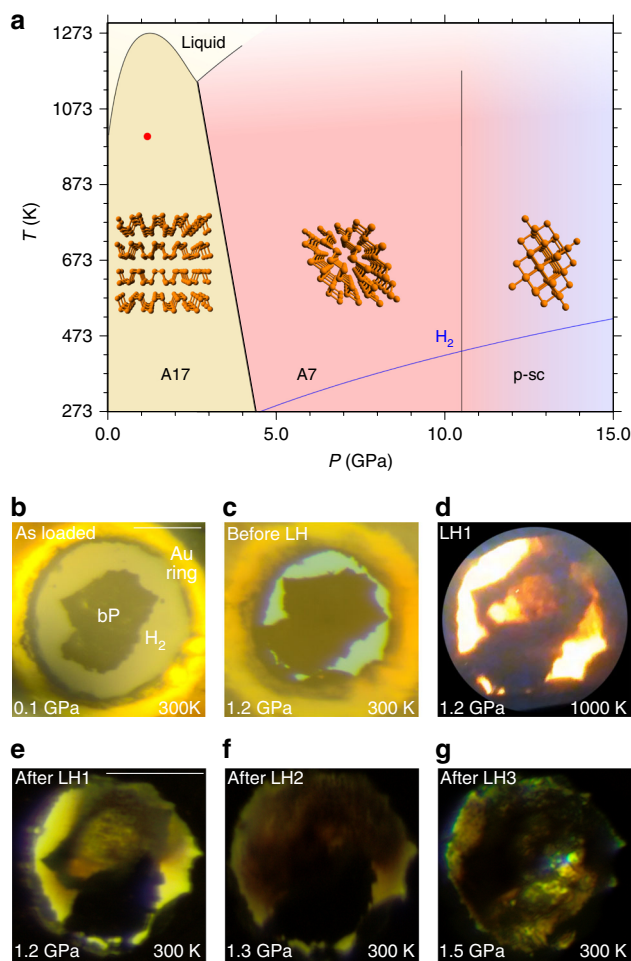


Fig. 1 Phase diagram and reactivity of P and H_2 at high pressure and high temperature. **a** Phase diagram of phosphorus (black lines), showing the stability regions of the orthorhombic (A17, P_{black}), rhombohedral (A7) and pseudo simple-cubic (p-sc) structures^{4,5}. The melting line of H_2 ⁷³ (blue line) and laser heating conditions (red point at $P = 1.2$ GPa, $T \approx 1000$ K) are also displayed. **b–g** Microphotographs showing the sample aspect after loading (**b**), before, during and after LH1 (**c–e**), after LH2 (**f**), and after LH3 (**g**) at pressure ranging between 1.2 and 1.5 GPa (LH1, LH2, and LH3, respectively, indicate the first, the second and the third laser heating). The scale bars in the top right corner of **b**, **e** correspond to 100 μm .

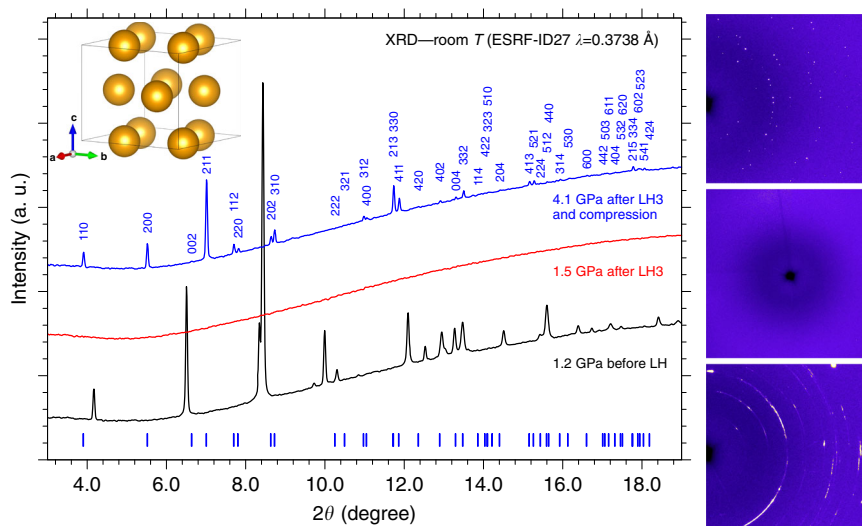


Fig. 2 X-ray diffraction. Integrated panoramic XRD patterns and corresponding detector images of the sample, acquired at room T before laser heating (LH) at 1.2 GPa (black trace, bottom image), after the third laser heating (LH3) at 1.5 GPa (red trace, middle image), and after compression at 4.1 GPa (blue trace, top image). The blue ticks and labels respectively refer to the refined peak positions of the crystalline product at this pressure (Supplementary Note 1) and to the corresponding h,k,l indexing. The tetragonal $I4cm$ structure of P atoms as obtained from single-crystal data at 5.5 GPa is also shown in the top left corner of the Figure (see the “X-Ray Diffraction” section).

excess H_2 to form the crystalline vdW compound $(PH_3)_2H_2$, whose identification has remarkable implications. Pressure was statically generated by means of membrane DAC and temperature by laser heating (LH), with P_{black} acting at the same time as reactant and laser absorber and H_2 as a reactant and pressure transmitting medium.

Results

X-Ray Diffraction. After loading (see “Methods”), the sample of P_{black} and H_2 was compressed to 1.2 GPa, where three laser irradiations were performed. The irradiations power (<3 W at laser output) and duration (up to ~ 30 s) were carefully increased up to visually observe the real time chemical transformation of the sample, which occurred in the 900 ± 100 K temperature interval, with only a slight pressure drift from 1.2 to 1.3 GPa, and then to 1.5 GPa, respectively, after the second (LH2) and third (LH3) irradiation (Fig. 1).

Each irradiation produced an increasing transformation of P_{black} , as confirmed by the intensity decrease of the P_{black} peaks in the diffraction patterns acquired before and after laser heating. After LH3 the absence of diffraction peaks indicated the complete consumption of P_{black} , suggesting the formation of an amorphous or liquid product in the laser heated area (Fig. 2).

The sample was then compressed at room T and between 3.5 and 4.1 GPa the sudden appearance of single diffraction spots in the detector image, observed up to the highest explored pressure (5.5 GPa), unambiguously marked the formation of a crystalline product (Fig. 2). A careful XRD mapping of the sample over a grid with $10 \mu m$ spacing was performed to identify the regions where single spot diffraction could be observed. These regions were further explored by higher resolution mapping ($4 \mu m$ spacing grid) and single-crystal patterns acquired on selected points of the laser heated area.

As H_2 is liquid below 5.7 GPa (Fig. 1) and H atoms are weak X-ray scatterers, only information about the P atoms could be evinced from our single-crystal data, whose structure solution at 5.5 GPa indicates a tetragonal structure ($a = 7.6075(6) \text{ \AA}$, $b = 7.6075(6) \text{ \AA}$, $c = 6.3303(13) \text{ \AA}$, $\alpha = 90^\circ$, $\beta = 90^\circ$, $\gamma = 90^\circ$, $V = 366.36(9) \text{ \AA}^3$, $Z = 8$) belonging to space group $I4cm$ (n. 108, C_{4v}^{10}), where the shortest distance between P atoms is 3.608 \AA (Fig. 2 and Supplementary

Note 1) and which does not correspond to any known structure of phosphorus. An equivalent solution corresponding to centrosymmetric space group $I4/mcm$ (n. 140, D_{4h}^{18}) was initially considered (see “Discussion”).

The first reaction product that we thought about was of course PH_3 . Unfortunately, even if PH_3 is expected to solidify at higher pressure with respect to NH_3 (1.0 GPa) due to the smaller electric dipole moment and to the absence of H-bonding^{45,46}, the solidification pressure of PH_3 at room T is unknown.

Furthermore, the high pressure structure of solid PH_3 is also unknown and only ambient pressure low T XRD data by Natta and Casazza dating back to 1930⁴⁷ are available in the literature, indicating that PH_3 crystallizes into a compact packing face centered cubic structure, possibly belonging to space group T_h^2 ($Pn\bar{3}$, $P2/n\bar{3}$, n. 201) or O_h^4 ($Pn\bar{3}m$, $P4_2/n\bar{3} 2/m$, n. 224), none of which is compatible with our single-crystal data (Supplementary Note 2).

Even considering the P positions in the $I4cm$ and $I4/mcm$ structures obtained from the single-crystal data as occupied by PH_3 molecules, some inconsistencies emerge with a compact packing structure. Indeed, assuming orientationally disordered spherical shaped PH_3 molecules in contact with each other, deriving the molecular volume using as molecular radius half of the shortest distance between P atoms ($(4/3)\pi(3.608/2)^3 = 24.592 \text{ \AA}^3$, in agreement with literature^{48,49}), and considering 8 molecules per unit cell, then a filled volume of 196.736 \AA^3 out of the 366.36 \AA^3 unit cell volume obtained from the single-crystal data can be estimated, corresponding to a 0.537 filling ratio, which is significantly lower than the 0.74 ratio expected for a close packing structure.

This occurrence, indicating the presence of free volume, which can not be accounted for by a compact packing of PH_3 , provided the first hints suggesting the presence of interactions between PH_3 molecules and a different composition of our reaction product, as indeed confirmed by the spectroscopic data.

Fourier Transform InfraRed absorption spectroscopy. The Fourier Transform InfraRed (FTIR) spectra acquired after LH3 at 6.7 GPa and at different pressures during decompression are shown in Fig. 3 with the relevant band frequencies listed in Table 1. At 6.7 GPa, infrared absorption maxima are observed

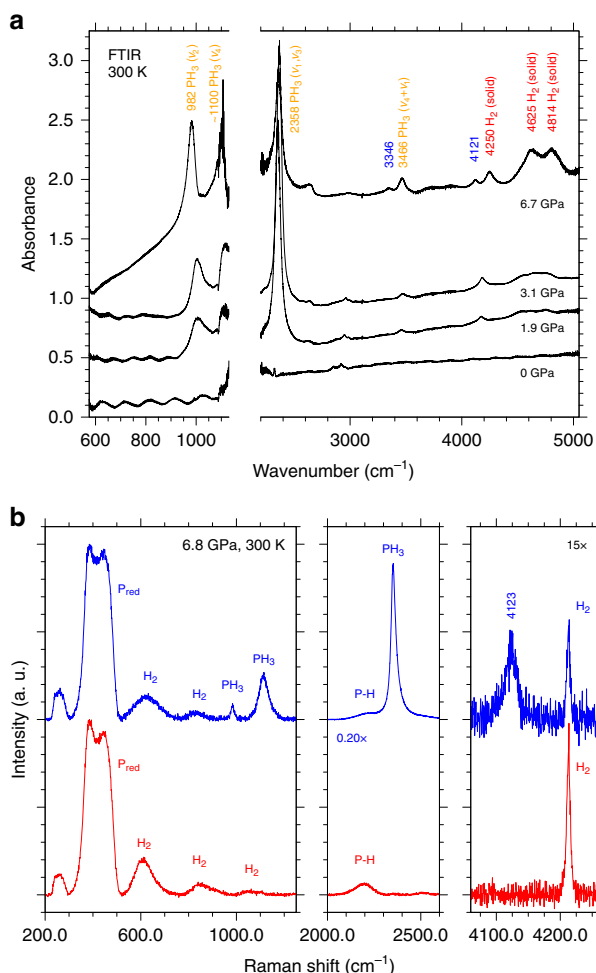


Fig. 3 FTIR and Raman spectroscopy. **a** Room T FTIR absorption spectra of the sample acquired at 6.7 GPa after LH3 and at different pressure values during decompression to ambient conditions. The two bands at 3346 and 4121 cm⁻¹ labeled in blue disappear on releasing pressure to 3.1 GPa. The spectra have been vertically translated for clarity and the values on the absorbance scale are intended for relative comparison. The break on the wavenumber axis excludes the spectral range corresponding to the *la* diamond saturating absorptions, which partially covers the ν₄ absorption of PH₃. The absorption features at ~2640 cm⁻¹ (6.7 GPa) and ~2900 cm⁻¹ (appearing on releasing pressure to 3.1 GPa) are assigned respectively to the diamond from the ambient pressure reference and to traces of oil on the optics of the interferometer. **b** Significant spectral regions of type-1 (red, lower trace) and type-2 (blue, upper trace) Raman spectra acquired on different selected spots of the mapping grid across the sample at 6.8 GPa and room T after LH. With respect to type-1 spectrum the type-2 one clearly shows the simultaneous presence of PH₃ and of the extra band at 4123 cm⁻¹ in the H₂ stretching region at lower frequency compared to pure H₂.

at 983, ~1100 (out of scale) 2358, 3346, 3466, 4121, 4250, 4625, and 4814 cm⁻¹.

The last three bands can be assigned to infrared active absorptions of H₂ (4250 (Q₁(1)), 4625 (Q₁(1)+S₀(0)), and 4814 (Q₁(1)+S₀(1)) cm⁻¹) in agreement with literature⁴⁴.

Even if the infrared bands of solid PH₃ have been measured only at low T^{50,51} and those of liquid PH₃ only at low temperature and modest high pressure (up to 35 atm)⁵², the bands observed at 983, ~1100, 2358, and 3466 cm⁻¹ can be confidently assigned to the fundamental and combination vibrational modes of PH₃, as indicated in Table 1.

Finally, the two remaining bands at 3346 and 4121 cm⁻¹ can not be assigned either to PH₃ or H₂ (Supplementary Note 3).

On decompression from 6.7 to 3.1 GPa, below the crystallization threshold of the reaction product, the two extra bands at 3346 cm⁻¹ and 4121 cm⁻¹ disappear. All the other bands of PH₃ exhibit a high-frequency shift, as typically observed in H-bonded systems when releasing pressure, and the bands of H₂ a low-frequency shift, as expected. On further decompression to ambient conditions, both PH₃ and H₂ bands shift to lower frequency, until disappearing with the opening of the cell.

No bands could be detected in the FTIR spectra after completely releasing the membrane pressure and opening/closing the cell under glove box in an inert atmosphere.

Raman spectroscopy. A detailed Raman mapping, consisting of a 130 × 130 μm² mesh with 10 μm grid spacing, was performed to gain insight about the reaction products and their spatial distribution within the sample at each pressure point during decompression, covering the entire frequency range between 40 and 4700 cm⁻¹. The analysis of the Raman spectra acquired across the sample at 6.8 GPa revealed the presence of two limit spectra, referred to in the following respectively as type-1 and type-2 Raman spectra, and a variety of combinations of them, with significant bands in three spectral regions: 200–1250 cm⁻¹, 2000–2600 cm⁻¹, and 4000–4300 cm⁻¹ (Fig. 3 and Supplementary Fig. 5).

Type-1 Raman spectrum (Fig. 3, lower panel, red trace) exhibits broad bands at 388, 449, 613, 833, 1064, 2198, 2520, and 4212 cm⁻¹, whereas in type-2 Raman spectrum additional bands are detected at 984, 1114, 2352, 4123 cm⁻¹. The two broad features observed in all the spectra at 388 and 449 cm⁻¹ can be assigned to amorphous P_{red} (Supplementary Note 5). The weak band at 2198 cm⁻¹, which has significantly lower frequency compared to phosphine (PH₃ 2321 cm⁻¹)⁵², or to higher phosphane homologues like diphosphane (P₂H₄ 2283 cm⁻¹)⁵³ and triphosphane (P₃H₅ 2267 cm⁻¹ at 193 K)⁵³, is compatible with the typical vibrational frequency of P–H bonds and further confirms the occurrence of chemical reactivity between P and H₂. The sharp band at 4212 cm⁻¹ identifies the characteristic stretching vibration of H₂ and those at 613, 833, and 1064 cm⁻¹ the corresponding pressure broadened S₀(1), S₀(2), and S₀(3) rotational bands (S₀(0) overlaps with the band of P_{red} at 388 cm⁻¹)⁵⁴.

Type-2 Raman spectrum exhibits additional bands at 984, 1114, and 2352 cm⁻¹, which can be readily assigned respectively to the ν₂, ν₄ and ν₁: ν₃ fundamental modes of PH₃⁵¹, consistently with the IR spectra (Fig. 3, lower panel, blue trace). However, differently from the IR spectra, no combination bands of PH₃ are detected in the Raman spectra. The Raman band at 4123 cm⁻¹, observed only in type-2 Raman spectra together with the presence of PH₃, almost exactly matches the corresponding IR absorption band at 4121 cm⁻¹ (6.7 GPa) and can not be assigned either to P, H₂ or PH₃.

As in the case of the IR spectra, during decompression to 3.1 GPa, below the crystallization pressure of the reaction product observed by XRD, the extra band at 4123 cm⁻¹ disappears, while the bands of PH₃ exhibit a high-frequency shift (Supplementary Fig. 5) and those of H₂ a low-frequency shift. Both PH₃ and H₂ bands frequencies all undergo a low-frequency shift on further decompression and disappear after opening the cell.

At 1.95 GPa three sharp bands, unambiguously identified as the characteristic A_g⁽¹⁾, E_g and A_g⁽²⁾ signatures of P_{black} respectively appear at 373, 443, and 467 cm⁻¹, remaining observable on decompression down to ambient pressure (Supplementary Fig. 5). Even if the detection of these three peaks could suggest an incomplete transformation of P_{black} and its missed observation, the

Table 1 Infrared absorption frequencies at different pressure values.

IR bands	6.7 (GPa)	3.1 (GPa)	1.9 (GPa)	0 (GPa)	gas ⁵²	Liquid ⁵²	solid (35 K) ⁵¹
PH ₃ $\nu_2(A_1)$ bend-s	983	1005	1002		992	-1100	980.3
PH ₃ $\nu_4(E)$ bend-as	-1100 ^a				1122	-1100	1095.4
PH ₃ $\nu_1(A_1)$ str-s, $\nu_3(E)$ str-s	2358	2365	-2350 ^a		2321 (ν_1) 2327 (ν_3)	2314	2303.6 (ν_1) 2311.3 (ν_3)
	3346						
PH ₃ ($\nu_1 + \nu_4$):($\nu_3 + \nu_4$)	3466 4121	3472	3458			3402	
H ₂ (Q ₁ (1))	4250	4184	4173				
H ₂ (Q ₁ (1)+S ₀ (0))	4625						
H ₂ (Q ₁ (1)+S ₀ (1))	4814						

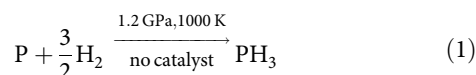
Infrared absorption frequencies acquired at different pressure values during decompression to ambient pressure. The peak position of the ν_4 band is not observable due to the overlap with the saturating absorption of the Ia diamond anvils. ν_1 and ν_3 are overlapped and unresolved. Literature values for PH₃ are also reported.
 bend bending, str stretching, -s symmetric, -as asymmetric.
^aOut of scale absorption.

Raman spectra acquired at 0.2 GPa and at ambient pressure on the recovered sample show characteristic bands at $\sim 385\text{ cm}^{-1}$, which is not present in any of the P_{red} forms nor in P_{black} (Supplementary Fig. 7), and at 2245 cm^{-1} in the P–H stretching region, which closely resemble the Raman spectra reported by Yuan and coauthors for the recovered products of the decomposition of PH₃ quenched from 25 GPa to 31 GPa⁵⁵ (Supplementary Fig. 8), thus suggesting a laser-induced decomposition of PH₃ during the acquisition of the Raman spectra, after releasing pressure below the crystallization threshold of the reaction product.

Interestingly, the P–H stretching band observed at 2200 cm^{-1} at 6.8 GPa exhibits a high-frequency shift to $\sim 2226\text{ cm}^{-1}$ on releasing pressure to 3.1 GPa, which further increases to 2245 cm^{-1} on releasing pressure to ambient conditions (Supplementary Fig. 5), providing evidence of the presence of H-bonding in the recovered solid product. Unfortunately, no additional insight could be gained on the recovered solid material responsible for type-1 Raman spectrum, which appears to consist of a hydrogenated (H-functionalized) mixture of amorphous P_{red} and crystalline P_{black} .

Discussion

Our data provide clear experimental evidence for direct high-pressure and high-temperature chemical reactivity between elemental P_{black} and H₂. The resulting formation of PH₃ according to the following chemical equation



represents the so far unreported catalyst-free phosphorus analogue of the nitrogen-based Haber-Bosch reaction for the synthesis of NH₃ (Supplementary Note 9).

Compressing PH₃ in excess H₂ at room T, between 3.5 and 4.1 GPa, the XRD data indicate the crystallization of a reaction product. As type-1 Raman spectrum was assigned to an amorphous solid product, we related the X-ray diffraction pattern of our crystalline product to type-2 Raman spectra, in which PH₃ is observed, and considered the P positions of the corresponding structure to be occupied by PH₃ molecules. The presence of PH₃ in type-2 Raman spectra is always associated to the detection of an extra band in the H₂ stretching region at lower frequency compared to pure H₂, which disappears on releasing pressure below the crystallization threshold of the crystalline reaction product. A similar behavior is observed in the IR spectra, where an extra band is detected at 4121 cm^{-1} (6.7 GPa), almost exactly coinciding with the frequency of the extra Raman band at 4123 cm^{-1} (6.8 GPa).

Whereas the sharp higher frequency band perfectly matches with the literature data about H₂ molecules in crystalline phase I

(4250 cm^{-1} in IR and 4212 cm^{-1} in Raman at 6.8 GPa)⁵⁶, the unassigned and unexpected broader extra band at lower frequency (4121 cm^{-1} at 6.7 GPa in IR and 4123 cm^{-1} at 6.8 GPa in Raman), indicates the presence of a second type of H₂ molecules, which experience a significant weakening of the bond force constant (5.15%, average value between 4.30% Raman and 6.00% IR weakening), likely due to a different local force field, as indeed consistently attested by their larger bandwidth in comparison to pure H₂.

A possible interpretation for this occurrence is the formation of a van der Waals crystalline compound made of PH₃ and H₂ molecules with (PH₃)₂H₂ stoichiometry and a tetragonal Al₂Cu-like structure belonging to $I4cm$ space group²⁶, where PH₃ and H₂ respectively occupy $8c$ (C_2) and $4a$ (C_4) Wyckoff sites (Fig. 4). In this structure four molecules of PH₃ are located on a plane parallel to the [a, b] direction at 0.5z and occupy the positions around a 4-fold rotation axis (C_4) along the c direction. Four additional molecules occupy the positions generated by a rotation along C_4 and a translation along +0.5z, giving rise to alternatively rotated layers of PH₃ molecules.

This interpretation of our data is in agreement with the $I4cm$ tetragonal structure of P atoms obtained from the single-crystal data and also accounts for the existence of free volume in the unit cell, in the case PH₃ only would be present.

Furthermore, in this structure the H₂ molecules are engaged within square antiprismatic voids delimited by eight PH₃ molecules (four on one layer and four on the adjacent layer) and occupy a single type of crystal site (C_4), corresponding to $4a$ Wyckoff positions, whose occupancy, according to group theory, is consistent with the appearance of one infrared and Raman active crystal component for the H₂ stretching vibration (Supplementary Note 6 and Supplementary Fig. 10).

In addition, the occupation by PH₃ molecules of $8c$ Wyckoff sites (C_2), is consistent with the splitting of the ($\nu_1 + \nu_4$):($\nu_3 + \nu_4$) combination band. The extra band observed in the IR spectra at 3346 cm^{-1} at 6.8 GPa, disappearing on decompression to 3.1 GPa, can be thus assigned to PH₃ molecules forming the (PH₃)₂H₂ crystal structure (Supplementary Note 6 and Supplementary Fig. 10).

A density of 1.269 g cm^{-3} can be calculated at 5.5 GPa from the refinement of the single-crystal data, with 2.89% in weight of H₂ and total 11.5% in weight of H (H₂ + H in PH₃).

The molecular nature of the reaction product is further confirmed by the bulk modulus $B = 6.7 \pm 0.8\text{ GPa}$ derived from the 2nd order Birch-Murnaghan equation of state in the investigated pressure range, which is in absolute agreement with analogous systems²⁶, and by the pressure evolution of the nearly constant c/a axial ratio, which indicates an almost isotropic compression within the applied pressure range (Supplementary Note 7).

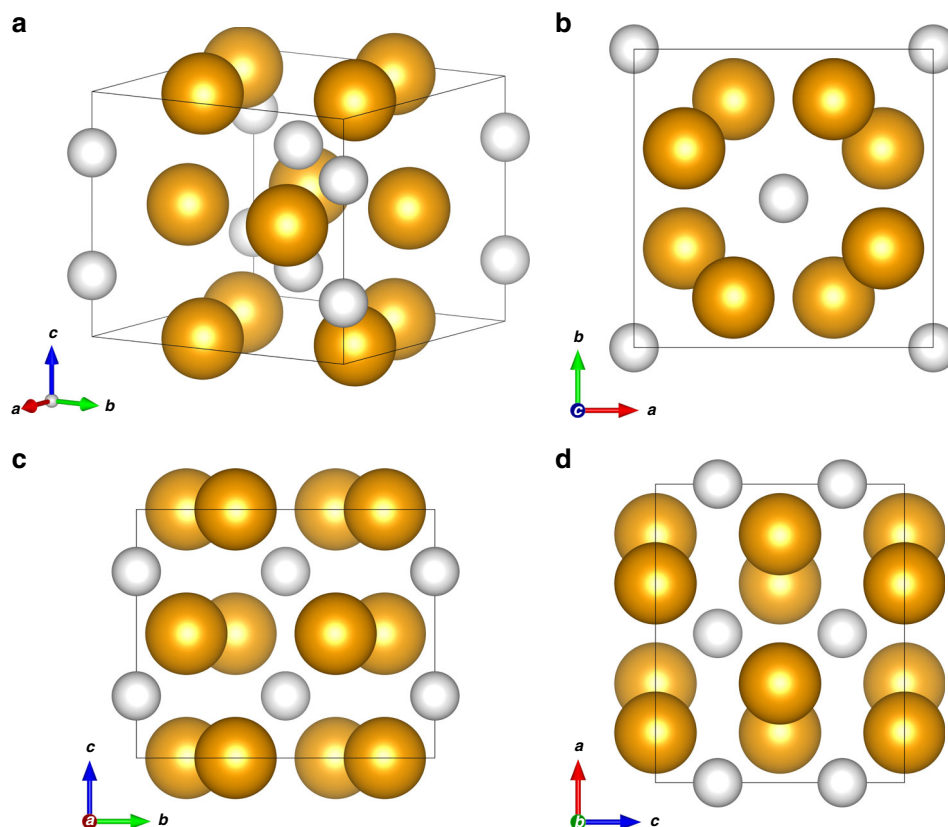


Fig. 4 Crystal structure of the $(\text{PH}_3)_2\text{H}_2$ vdW compound. Crystal structure of the $(\text{PH}_3)_2\text{H}_2$ vdW compound at 5.5 GPa and room T **(a)** with views along the c **(b)**, a **(c)**, and b **(d)** crystal axes. The orange spheres represent the PH_3 molecules, whereas the white spheres represent the H_2 molecules. The size of the spheres has been drawn by estimating their radius as the sum of the P–H bond length (1.421 \AA)² and H van der Waals radius (1.20 \AA)⁴⁹ in the case of PH_3 (2.62 \AA) and as the sum of the H van der Waals radius (1.20 \AA)⁴⁹ and half of the H–H distance (0.742 \AA)⁷⁴ in the case of H_2 (1.571 \AA).

Pressure has greatly extended the number of known hydrides synthesized under high-density conditions^{15,33}. Among non metallic elements, H_2 -containing hydrides have been reported so far in literature for elements ranging from group 14 to group 18 of the periodic table, and include van der Waals hydrides of noble gases, simple diatomic molecules, and covalent molecular hydrides (Supplementary Fig. 16).

If among these hydrides we only consider those involving elements which are able to form covalent molecular hydrides (Supplementary Fig. 17) and particularly focus on those which have been reported to adopt a $I4cm$ ($I4/mcm$) crystal structure with X_2H_2 composition, where X represents the corresponding molecular hydride (Supplementary Fig. 18), then we observe that this structure has been experimentally reported in the case of: carbon, with methane (CH_4)¹⁹, for group 14; sulphur, with H_2S ²⁶, and selenium, with H_2Se ²⁷, for group 16; and iodine, with HI ⁵⁷, for group 17. Interestingly, to the best of our knowledge no such structure has been reported so far for any of the elements of group 15.

In particular $(\text{CH}_4)_2\text{H}_2$, $(\text{H}_2\text{S})_2\text{H}_2$, $(\text{H}_2\text{Se})_2\text{H}_2$ and $(\text{HI})_2\text{H}_2$ all reportedly exhibit the same $I4/mcm$ structure, with the H_2 and X molecules respectively occupying $4a$ and $8h$ Wyckoff positions, whereas $(\text{PH}_3)_2\text{H}_2$ exhibits a $I4cm$ structure with the H_2 and PH_3 molecules occupying the $4a$ and $8c$ Wyckoff positions. The $I4cm$ and $I4/mcm$ structures are closely related and only differ for the presence of an inversion center in $I4/mcm$, with identical lattice parameters and atomic positions. Noticeably, even if the occupation of $8h$ Wyckoff positions of C_{2v} site symmetry by CH_4 , H_2S , H_2Se and HI , respectively in $(\text{CH}_4)_2\text{H}_2$, $(\text{H}_2\text{S})_2\text{H}_2$, $(\text{H}_2\text{Se})_2\text{H}_2$ and

$(\text{HI})_2\text{H}_2$ does not rise any symmetry issue (such as in the case of PH_3 (C_{3v}) occupying a C_{2v} site in the $I4/mcm$ structure), no infrared spectra for any of these compounds have been acquired in the H_2 stretching region, where, according to the analysis of the Davydov components activity using group theory arguments, the appearance of an extra band would unambiguously support the formation of a structure belonging to the $I4cm$ rather than to the $I4/mcm$ space group (Supplementary Note 6). Indeed, the possibility of the $I4cm$ lower symmetry structure has been proposed also for $(\text{H}_2\text{S})_2\text{H}_2$ ²⁶, whereas the $I4/mcm$ structures of $(\text{H}_2\text{Se})_2\text{H}_2$ and $(\text{HI})_2\text{H}_2$ were assigned according to similarity with $(\text{H}_2\text{S})_2\text{H}_2$, thus suggesting all these structures to belong to $I4cm$ rather than $I4/mcm$ space group. Furthermore, the consistency of the IR and Raman optical activity with the application of group theory to the crystal symmetry, indicates that the PH_3 molecules are not randomly oriented and that their orientations reflect the symmetry and periodicity of the intermolecular potential originating from their symmetry. This apparently contrasts with the orientational disorder reported for CH_4 , H_2S , H_2Se , and HI , respectively, in $(\text{CH}_4)_2\text{H}_2$, $(\text{H}_2\text{S})_2\text{H}_2$, $(\text{H}_2\text{Se})_2\text{H}_2$, and $(\text{HI})_2\text{H}_2$, which has been speculated from the behavior of the pure hydrides, without any conclusive evidence to support it like IR absorption spectra in the H_2 stretching region (Supplementary Note 10)^{58,59}.

The identification of $(\text{PH}_3)_2\text{H}_2$ thus represents the discovery of the missing tile for group 15, specifically corresponding to phosphorus, in the puzzle of the periodic properties of non-metallic elements, which are able to form van der Waals molecular compounds containing their covalent hydrides and H_2 molecules (Fig. 5).

18

					2 He Helium
5 B Boron	6 C Carbon	7 N Nitrogen	8 O Oxygen	9 F Fluorine	10 Ne Neon
13 Al Aluminium	14 Si Silicon	15 P Phosphorus	16 S Sulphur	17 Cl Chlorine	18 Ar Argon
31 Ga Gallium	32 Ge Germanium	33 As Arsenic	34 Se Selenium	35 Br Bromine	36 Kr Krypton
49 In Indium	50 Sn Tin	51 Sb Antimony	52 Te Tellurium	53 I Iodine	54 Xe Xenon
81 Tl Thallium	82 Pb Lead	83 Bi Bismuth	84 Po Polonium	85 At Astatine	86 Rn Radon

Fig. 5 The missing tile of P for group 15. Non-metal region of the Periodic Table showing the elements (yellow and orange) able to form crystalline X_2H_2 vdW compounds ($X = CH_4^{19}$, PH_3 , H_2S^{26} , H_2Se^{27} , HI^{57}) having the $I4cm$ ($I4/mcm$) structure, with P ($X = PH_3$), highlighted in orange, representing the so far missing tile for group 15 elements reported in this study (see text).

Hydride	P (GPa)	ν_{H-H} (X_2H_2)	ν_{H-H} (H_2)	$\Delta\nu$
CH_4	5.4	-	-	+13
PH_3	6.8	4121	4213	-92
H_2S	7.0	4147	4213	-66
H_2Se	7.0	4106	4213	-107
HI	6.8	4162	4213	-51

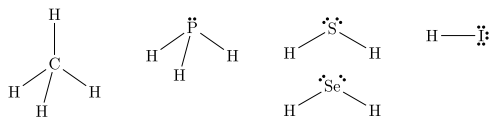


Fig. 6 Raman shift of the H_2 stretching vibration in different isostructural X_2H_2 compounds. Upper panel. Table reporting the Raman frequency (cm^{-1}) of the H-H stretching vibration of H_2 molecules in different isostructural X_2H_2 crystals (ν_{H-H} (X_2H_2)) with $X = CH_4^{19}$, PH_3 , H_2S^{26} , H_2Se^{27} , and HI^{57}) and their frequency shift ($\Delta\nu$) with respect to bulk H_2 (ν_{H-H} (H_2)) in comparable pressure conditions. Ref. ¹⁹ directly provides the frequency shift value for CH_4 . Lower panel. The molecular structures of CH_4 , PH_3 , H_2S , H_2Se , and HI, drawn according to the VSEPR theory and fulfilling the octet rule for the electron outer shell, are shown to highlight the absence of lone pairs on C in CH_4 , comparing to the other hydride forming elements.

A further chemical insight can be gained from the Raman data. All these five X_2H_2 isostructural compounds feature the extra Raman band in the H_2 stretching region, due to the vibration of the H_2 molecules inside their structure, in addition to the signal of the surrounding pure H_2 , which is always present as excess reactant from the synthesis. These frequencies are listed in the Table in Fig. 6, together with the corresponding frequency shift with respect to pure H_2 . An interesting feature emerging from this comparison is that, at similar high-pressure conditions, the frequency shift of the extra band with respect to pure H_2 is always negative, except in the case of methane. According to the valence shell electron pair repulsion (VSEPR) theory, and to the fulfillment of the octet rule for the outer electronic shell⁴⁵, the main difference between methane and the other hydrides is that

methane does not possess an electron lone pair on carbon, whereas PH_3 , H_2S , H_2Se and HI all have at least one electron lone pair on the hydride forming element (Fig. 6).

The presence of lone pairs is typically associated to the ability of forming H-bonding, as indeed observed for all these systems, and of behaving as an electron donor Lewis base. H-bonding between the corresponding hydride molecules, evidenced by a negative frequency shift with increasing pressure of the internal stretching modes involving H atoms, has been indeed reported for $(H_2S)_2H_2$, $(H_2Se)_2H_2$, and $(HI)_2H_2$.

The high-frequency shift, observed both in the infrared and Raman spectra acquired on releasing pressure from 6.8 to 3.1 GPa across the melting threshold of the crystalline product (Supplementary Fig. 6), suggests also PH_3 to behave like the analogous X_2H_2 isostructural van der Waals compounds, exhibiting $H_3P \cdots H-PH_2$ H-bonding interactions, which disappear on decompression from 6.8 to 3.1 GPa after the decomposition of $(PH_3)_2H_2$, as attested by the decrease of the vibrational frequencies of PH_3 on further decompression.

The presence of a H-bonding between PH_3 molecules has noticeable chemical relevance as PH_3 , in contrast to NH_3 , is known for not forming H-bonding at ambient conditions^{45,46}, due to the small electronegativity difference of phosphorus with respect to hydrogen and to the consequent smaller electric dipole moment⁶⁰. Furthermore, the existence of such interaction, together with the presence of H_2 molecules, is in agreement with the larger volume of the crystalline cell of $(PH_3)_2H_2$ compared to what expected in pure PH_3 .

The softening of the stretching vibration in the H_2 molecules forming the $(PH_3)_2H_2$ crystal clearly indicates the presence of chemical interaction between H_2 and PH_3 . In the case of the isolated molecules such interaction has been described by ab initio computational methods⁶¹ in terms of two possible contributions: 1) the electron lone pair of P can act as a Lewis base and the σ^* anti-bonding molecular orbital of H_2 as a Lewis acid ($n \rightarrow \sigma^*$); 2) the σ bonding molecular orbital electrons of H_2 act as Lewis base and the first anti-bonding molecular orbital of PH_3 as a Lewis acid ($\sigma \rightarrow \sigma^*(H-PH_2)$).

The first interaction is essentially a HOMO-LUMO orbital overlap interaction involving the highest occupied molecular orbital (HOMO) of PH_3 ($2a_1$ symmetry), which hosts the electron lone pair and has a prevalent non-bonding character, and the unoccupied σ^* anti-bonding molecular orbital of H_2 , technically the lowest unoccupied molecular orbital (LUMO), whereas the second one corresponds to the opposite situation, where the HOMO σ bond electron density of H_2 interacts with the LUMO orbital of PH_3 ($3a_1$) (Fig. 7). Energetically, the first interaction is larger when the $2a_1$ HOMO of PH_3 and the σ^* of H_2 have maximum overlap, with the electron lone pair and the molecular axis of H_2 aligned, but is present, even to a smaller extent, also in other interaction configurations, whereas the second one requires the σ electron density of H_2 to interact with the $3a_1$ LUMO of PH_3 in a configuration where the electron lone pair is perpendicular to H_2 molecular axis.

In solid state, as group 15 elements are concerned, the first kind of interaction has been recently reported to be responsible for the softening of the H_2 stretching vibration in the $As_4O_6 \cdot 2H_2$ crystal by electron density transfer from the As electron lone pair to the σ^* anti-bonding orbital of H_2 ⁶². Gúnka et al. achieved this result by adopting the ICOHP (integrated projected crystal orbital Hamilton population) and ICOOP (integrated projected crystal orbital overlap population) computational methods, which, based on the crystal orbital overlap population (COOP) approach originally developed by R. Hoffmann⁶³, indeed relate the local molecular orbitals to the band structure of crystals through the projection decomposition of the electron density of states,

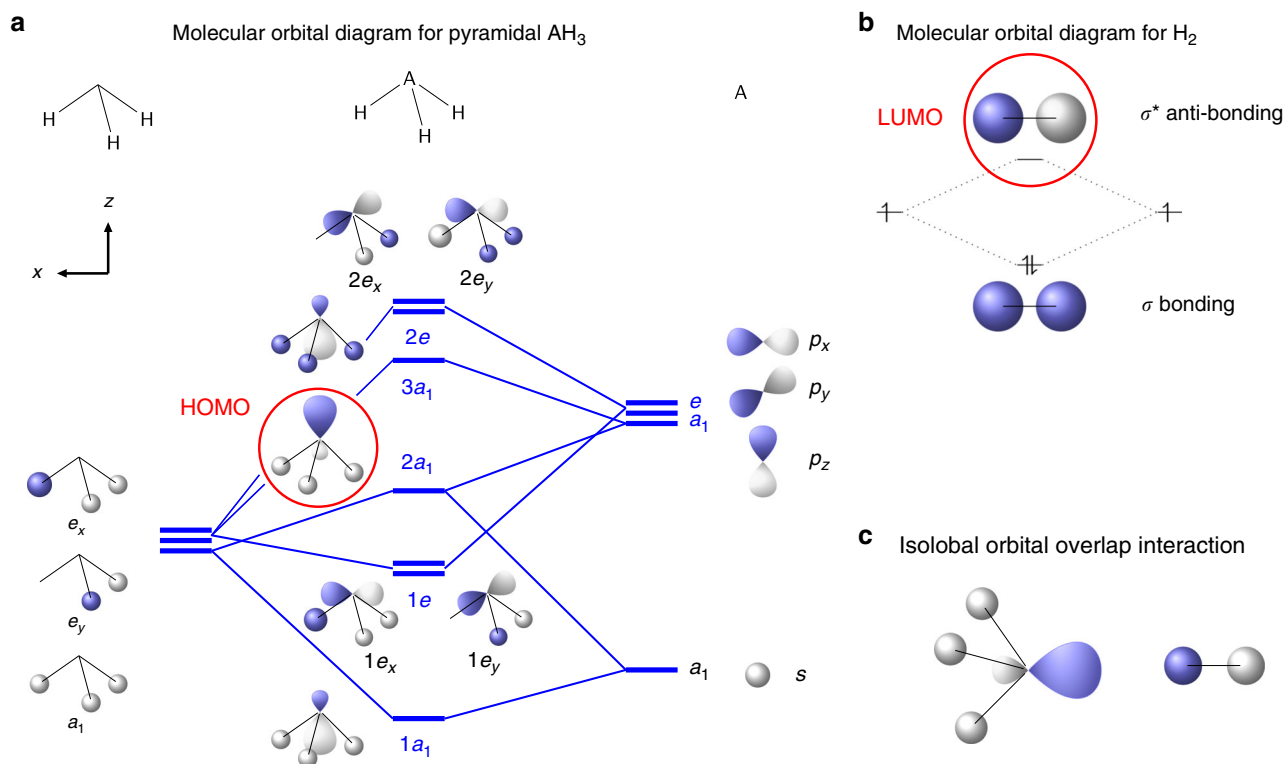


Fig. 7 The molecular orbital interaction between PH_3 and H_2 in $(\text{PH}_3)_2\text{H}_2$. **a** Qualitative molecular orbital diagram for pyramidal AH_3 (where $\text{A} = \text{N}, \text{P}, \text{Sb}, \text{Bi}$) obtained from the symmetry adapted linear combination of atomic orbitals of H_3 (C_{3v}) and A fragments (adapted from Figures 4–9 in ref. ⁷⁵). The orbitals of each fragment are aligned vertically, in order of increasing energy from bottom to top, under the corresponding column of panel a, with H_3 on the left side, AH_3 in the middle and A on the right side. The $2a_1$ highest occupied molecular orbital (HOMO), where the electron lone pair is located, is highlighted by a red circle. **b** Molecular orbital diagram for H_2 , showing the completely filled σ bonding molecular orbital and the empty σ^* anti-bonding lowest unoccupied molecular orbital (LUMO) highlighted by a red circle. **c** Isolobal orbital overlap interaction between the $2a_1$ molecular orbital of AH_3 and the σ^* anti-bonding molecular orbital of H_2 .

allowing to gain insight about the frontier orbitals that control structure and reactivity in extended systems.

Accordingly, a qualitative interpretation for the softening of the stretching vibration of the H_2 molecules in the $(\text{PH}_3)_2\text{H}_2$ crystal, certainly deserving appropriate theoretical investigation for effective electronic band structure calculation, is here proposed in terms of isolobal frontier molecular orbital overlap interaction between the HOMO of PH_3 , hosting the electron lone pair, and the σ^* anti-bonding LUMO of H_2 (Fig. 7). Even if the orientation of PH_3 and H_2 molecules is not known, considering that H_2 is expected to undergo hindered rotations at this pressure, it is indeed likely that the $2a_1$ HOMO of some of the PH_3 molecules building up the cavities, where the H_2 molecules are hosted, and the σ^* anti-bonding orbital of H_2 dynamically adopt the correct orientation for an effective overlap. The σ^* anti-bonding orbital of H_2 is normally not occupied, which makes the H_2 molecule stable. The electron density transfer from the lone pair of PH_3 to the σ^* anti-bonding orbital of H_2 may decrease the bonding electron density of the H_2 molecule, thus causing a reduction of the force constant ($\sim 5.15\%$) and finally a frequency decrease of the H_2 stretching mode, according to the harmonic oscillator frequency equation ($\nu = \frac{1}{2\pi} \sqrt{\frac{k}{\mu}}$). The existence of the $\sigma(\text{H}_2) \rightarrow \sigma^*(\text{H-PH}_2)$ interaction may further contribute to this effect. As a result, the H_2 molecules within the crystal structures of $(\text{PH}_3)_2\text{H}_2$ exhibit a lower vibrational frequency compared to bulk solid H_2 .

Finally, the observation of $(\text{PH}_3)_2\text{H}_2$ is also somehow relevant for superconductivity in PH_3 . PH_3 has been experimentally reported to become metallic at 40 GPa and superconducting at

207 GPa with a T_c of 103 K, but with no structural characterization so far³⁶. Since then quite a lot of theoretical efforts have been made to account for such observation. At the moment, theory and experiments seem to agree about the instability of pure PH_3 at high pressure, whose decomposition proceeds through the release of H_2 . Experimentally, a couple of recent papers have reported the decomposition of PH_3 ^{55,64}, with the initial formation of diphosphane followed by decomposition into elemental phosphorus and H_2 . However, no further convincing characterization was proposed, suggesting that, like in the case of H_2S , other species may be responsible for the superconductivity observed by Drozdov et al.³⁶. Theoretically, besides predicting the decomposition of PH_3 , different studies have calculated the stabilization of PH_2 phases above 80 GPa, which, from a stoichiometric point of view, is consistent with the release of H_2 ^{37,38}. Furthermore, a key role of molecular H_2 in stabilizing the high-pressure superconducting phases of phosphorus hydrides has been recently proposed³⁹. Interestingly, even if the pressure range is here much lower, our data show that PH_3 and H_2 form a crystalline vdW compound, in which molecular H_2 is indeed involved, possibly stabilizing PH_3 , or other related species, even at higher pressure.

To summarize, the results of this study have multiple chemically relevant implications. First of all, using LH in DAC, we have successfully induced direct reactivity between P_{black} and H_2 at 1.2 GPa and temperature lower than 1000 K, without the use of any catalyst or precursor. To our knowledge this is the first report about a direct chemical reaction between P_{black} , the thermodynamically stable allotrope of P, and H_2 at high pressure and

high temperature to form PH_3 , somehow mimicking and representing the P analogue of the Haber-Bosch process for the synthesis of NH_3 from N_2 and H_2 .

Secondly, at room T and pressure between 3.5 and 4.1 GPa PH_3 combines with excess H_2 to form the crystalline $(\text{PH}_3)_2\text{H}_2$ van der Waals compound, whose observation consistently fills a gap existing for pnictogens in the periodic properties of non-metallic elements able to form crystalline vdW compounds made of the corresponding hydride and of molecular hydrogen. The identification of $(\text{PH}_3)_2\text{H}_2$ represents the so far missing tile of P in this puzzle and confirms a general trend in the formation of H_2 -containing vdW compounds with X_2H_2 stoichiometry (X = molecular hydride) and *I4cm* (*I4/mcm*) structure.

The formation of unexpected chemical compounds made of components apparently non-interacting at ambient conditions, such as P and H, is extremely important for their relevant implications, which include H_2 storage, the chemistry occurring in extraterrestrial environments of giant planets such as Jupiter, Saturn, and their moons, where PH_3 and H_2 are present^{40,41,43}, and the identification of astrochemical processes leading to the synthesis of phosphine, which is a critical issue for the detection of the presence of life in harsh extraterrestrial environments of rocky planets, as inferred by the recent observation of anomalous high levels of phosphine in the cloud decks of Venus atmosphere⁶⁵.

Third, as advancement in fundamental bond theory is concerned, the relevant observation of H-bonding in PH_3 , which in contrast to NH_3 is not reported to exist at ambient pressure, and the existence of a molecular orbital interaction between the electron lone pair in PH_3 and the antibonding molecular orbital of H_2 , provide remarkable insights to understand the effects underlying the predicted stabilization of the P–H systems under high-pressure conditions.

Finally, the synthesis of $(\text{PH}_3)_2\text{H}_2$ effectively provides confirmatory experimental evidence for the key role played by H_2 molecules in stabilizing the PH system at high pressure, as suggested by recent calculations predicting the presence of H_2 units in superconducting PH structures at high pressure.

Once again the history of phosphorus has intertwined with pressure, whose role in enhancing similarities and consistencies in the periodic properties of elements apparently exhibiting particular behavior at ambient conditions^{5,66,67} is here further highlighted.

Methods

Synthesis of P_{black} . Pure crystalline P_{black} was synthesized from red phosphorus according to reference⁶⁸. All the reactants used for the synthesis of P_{black} were purchased from Sigma-Aldrich with the following purity: red phosphorus (>99.99%), tin (>99.999%), gold (>99.99%), and SnI_4 (99.999%). The purity of the synthesized P_{black} crystals was checked by X-ray powder diffraction, Raman spectroscopy, EDX analysis and ICP-MS measurements, the latter giving a purity of 99.999+%. The crystals of P_{black} were fragmented by means of a metallic tip for obtaining smaller 20–40 μm chips to be loaded into the DAC.

Sample preparation and the experimental conditions. Pressure was generated by means of membrane Diamond Anvil Cells (DAC) equipped with Ia type standard cut 16-sided beveled anvils having 600 μm culets. Re gaskets 200 μm thick were indented to 80 μm thickness and laser-drilled to obtain a 300 μm sample chamber. Before using them for the sideways containment of the samples, a Au ring was applied to prevent unintended catalytic effect and H_2 diffusion and reactivity with Re. For this purpose the 300 μm diameter gasket hole was filled with Au powder, compressed with ~20 bar of He in the membrane until the powder appeared reflective and then laser-drilled again to obtain a 250 μm diameter hole. A small crystal of P_{black} was placed in the sample chamber by means of a metallic tip and the remaining volume was filled with fluid H_2 using standard gas-loading technique. Au and a ruby chip were used to measure the pressure, whereas the temperature was measured by the fit of the black body thermal radiation emission of the sample during laser heating. High temperature was generated by means of Nd:YAG laser source ($\lambda = 1064 \text{ nm}$) focused on the P_{black} crystal ($\approx 30 \mu\text{m}$ beam spot size diameter), which acted both as reactant and laser absorber, thus avoiding any

other source of contamination. No evidence for the formation of Au^{69} or Re^{70} hydrides was observed.

X-ray diffraction data acquisition and analysis. XRD experiments were carried out at the ESRF-ID27 beamline using a monochromatic synchrotron radiation beam ($\lambda = 0.3738 \text{ \AA}$) focused to $\sim 5 \mu\text{m}$ to select different areas of the heterogeneous sample. The diffracted radiation was revealed by a MAR CCD165 detector, located approximately at 187 mm from the sample. The setup was calibrated against a CeO_2 powder standard and Dioptas software was used to integrate the 2D area images to 1D patterns.

A single-crystal data set was collected at 5.5 GPa. Diffraction intensities were acquired in an ω -oscillation scan mode over the range $\pm 30^\circ$ with a frame width of 0.5° and an exposure time of 2 s per single frame. The instrument model was calibrated at the beginning of the beam time by performing a full data collection of an enstatite single-crystal placed in a dummy DAC. The diffraction images were then imported into a CrysAlisPro suite (Supplementary Note 1) and processed accordingly. After determining the unit cell the intensities were reduced applying corrections for Lorentz and polarization effects, and also a multiscan absorption correction at the final step. Reciprocal lattice layers were reconstructed using the unwarped procedure (Supplementary Fig. 1). Careful inspection of the unwarped images did not reveal any twinning, satellite reflections or diffuse scattering, in contrast to the crystal of $(\text{H}_2\text{Se})_2\text{H}_2$, where diffuse scattering streaks were observed²⁷. The crystal structure was subsequently solved by direct methods and then refined on F^2 by full-matrix least-squares procedures using the SHELXL package (Supplementary Note 1). In addition, at the same pressure and at two other pressure points (4.1 and 4.5 GPa), panoramic oscillation images ($\phi = \pm 5^\circ$, acquisition time 30 s) of oligocrystalline conglomerate were recorded and used to perform Le Bail fits with JANA 2006 software after azimuthal integration (Supplementary Figs. 2–4).

Spectroscopic data acquisition and analysis. The Raman spectra were acquired at LENS with 1.5 cm^{-1} spectral resolution using the 647.1 nm emission wavelengths of a Kr ion laser. The details of the Raman setup are described elsewhere⁷¹. Raman spectra were acquired performing a 14×14 mapping over a $10 \mu\text{m}$ spaced grid using a single 300 groove/mm grating, which allowed to cover the 200–3300 cm^{-1} frequency region with 4 cm^{-1} spectral resolution. The most significant spots of the mapping were further inspected at higher resolution (1.5 cm^{-1}) with different grating configuration down to 23.5 cm^{-1} (triple grating subtractive configuration 900–900–1800 groove/mm) and up to 4700 cm^{-1} (single grating configuration 900 groove/mm). No photochemical effect was observed at the employed laser power (1.5 mW) for pressure higher than 1.9 GPa, whereas at this pressure the formation of P_{black} could indicate the decomposition of PH_3 ⁵⁵.

The FTIR spectra were acquired with 1 cm^{-1} spectral resolution, using a Bruker IFS-120HR interferometer, suitably modified for the acquisition of infrared absorption spectra at high pressure in DAC⁷².

The frequency and intensity of the FTIR and Raman bands were obtained by fitting procedure using Voigt line shapes after baseline subtraction. Fityk software was used for this purpose.

Data availability

The X-ray crystallographic coordinates for the structure of the $(\text{PH}_3)_2$ vdW compound reported in this study have been deposited at the Cambridge Crystallographic Data Centre (CCDC), under deposition number 2034375. These data can be obtained free of charge from The Cambridge Crystallographic Data Centre via www.ccdc.cam.ac.uk/dataservice/cif. All other data that support the findings of this study are available from the corresponding author upon reasonable request.

Received: 7 March 2020; Accepted: 14 October 2020;

Published online: 30 November 2020

References

1. Bridgman, P. W. Two new modifications of phosphorus. *J. Am. Chem. Soc.* **36**, 1344–1363 (1914).
2. Corbridge, D. *Phosphorus: Chemistry, Biochemistry and Technology, Sixth Edition.* (Taylor & Francis, 2013).
3. Jamieson, J. C. Crystal structures adopted by black phosphorus at high pressures. *Science* **139**, 1291–1292 (1963).
4. Scelta, D. et al. Interlayer bond formation in black phosphorus at high pressure. *Angew. Chem. Int. Ed.* **56**, 14135–14140 (2017).
5. Scelta, D. et al. The p-sc structure in phosphorus: bringing order to the high pressure phases of group 15 elements. *Chem. Commun.* **54**, 10554–10557 (2018).
6. Peruzzini, M. et al. A perspective on recent advances in phosphorene functionalization and its applications in devices. *Eur. J. Inorg. Chem.* **2019**, 1476–1494 (2019).

7. Ryder, C. R. et al. Covalent functionalization and passivation of exfoliated black phosphorus via aryl diazonium chemistry. *Nat. Chem.* **8**, 597–602 (2016).
8. Bódi, D. & Höltzl, T. Thermal stability and flexibility of hydrogen terminated phosphorene nanoflakes. *J. Phys. Chem. C* **122**, 8535–8542 (2018).
9. Mao, H.-K., Chen, X.-J., Ding, Y., Li, B. & Wang, L. Solids, liquids, and gases under high pressure. *Rev. Mod. Phys.* **90**, 015007 (2018).
10. Citroni, M., Ceppatelli, M., Bini, R. & Schettino, V. Laser-induced selectivity for dimerization versus polymerization of butadiene under pressure. *Science* **295**, 2058–2060 (2002).
11. Chelazzi, D., Ceppatelli, M., Santoro, M., Bini, R. & Schettino, V. High-pressure synthesis of crystalline polyethylene using optical catalysis. *Nat. Mater.* **3**, 470–475 (2004).
12. Dong, X. et al. A stable compound of helium and sodium at high pressure. *Nat. Chem.* **9**, 440–445 (2017).
13. Dewaele, A. et al. Synthesis and stability of xenon oxides Xe_2O_5 and Xe_3O_2 under pressure. *Nat. Chem.* **8**, 784–790 (2016).
14. Howie, R. T., Turnbull, R., Binns, J., Frost, M., Dalladay-Simpson, P. & Gregoryanz, E. Formation of xenon-nitrogen compounds at high pressure. *Sci. Rep.* **6**, 34896 (2016).
15. Wang, H., Li, X., Gao, G., Li, Y. & Ma, Y. Hydrogen-rich superconductors at high pressures. *Wiley Interdiscip. Rev. Comput. Mol. Sci.* **8**, e1330 (2018).
16. Mao, W. L. & Mao, H.-k. Hydrogen storage in molecular compounds. *Proc. Natl Acad. Sci. USA* **101**, 708–710 (2004).
17. Struzhkin, V. V., Miltzer, B., Mao, W. L., Mao, H.-K. & Hemley, R. J. Hydrogen storage in molecular clathrates. *Chem. Rev.* **107**, 4133–4151 (2007).
18. Vos, W. L. et al. A high-pressure van der Waals compound in solid nitrogen-helium mixtures. *Nature* **358**, 46–48 (1992).
19. Somayazulu, M. S., Finger, L. W., Hemley, R. J. & Mao, H. K. High-pressure compounds in methane-hydrogen mixtures. *Science* **271**, 1400–1402 (1996).
20. Strobel, T. A., Somayazulu, M. & Hemley, R. J. Novel pressure-induced interactions in silane-hydrogen. *Phys. Rev. Lett.* **103**, 065701 (2009).
21. Strobel, T. A., Chen, X.-J., Somayazulu, M. & Hemley, R. J. Vibrational dynamics, intermolecular interactions, and compound formation in $\text{GeH}_4\text{-H}_2$ under pressure. *J. Chem. Phys.* **133**, 164512 (2010).
22. Laniel, D., Svilyk, V., Weck, G. & Loubeyre, P. Pressure-induced chemical reactions in the $\text{N}_2(\text{H}_2)_2$ compound: from the N_2 and H_2 species to ammonia and back down into hydrazine. *Phys. Chem. Chem. Phys.* **20**, 4050–4057 (2018).
23. Ciezak, J. A., Jenkins, T. A. & Hemley, R. J. Optical and Raman microspectroscopy of nitrogen and hydrogen mixtures at high pressure. *AIP Conf. Proc.* **1195**, 1291–1294 (2009).
24. Loubeyre, P. & LeToullec, R. Stability of O_2/H_2 mixtures at high pressure. *Nature* **378**, 44–46 (1995).
25. Vos, W. L., Finger, L. W., Hemley, R. J. & Mao, H.-K. Novel $\text{H}_2\text{-H}_2\text{O}$ clathrates at high pressures. *Phys. Rev. Lett.* **71**, 3150–3153 (1993).
26. Strobel, T. A., Ganesh, P., Somayazulu, M., Kent, P. R. C. & Hemley, R. J. Novel cooperative interactions and structural ordering in $\text{H}_2\text{S-H}_2$. *Phys. Rev. Lett.* **107**, 255503 (2011).
27. Pace, E. J. et al. Synthesis and stability of hydrogen selenide compounds at high pressure. *J. Chem. Phys.* **147**, 184303 (2017).
28. Binns, J. et al. Synthesis and stability of hydrogen iodide at high pressures. *Phys. Rev. B* **96**, 144105 (2017).
29. Ulivi, L., Bini, R., Loubeyre, P., LeToullec, R. & Jodl, H. J. Spectroscopic studies of the $\text{Ar}(\text{H}_2)_2$ compound crystal at high pressure and low temperatures. *Phys. Rev. B* **60**, 6502–6512 (1999).
30. Kleppe, A. K., Amboage, M. & Jephcoat, A. P. New high-pressure van der Waals compound $\text{Kr}(\text{H}_2)_4$ discovered in the krypton-hydrogen binary system. *Sci. Rep.* **4**, 4989 (2014).
31. Somayazulu, M. et al. Pressure-induced bonding and compound formation in xenon-hydrogen solids. *Nat. Chem.* **2**, 50–53 (2010).
32. Somayazulu, M., Dera, P., Smith, J. & Hemley, R. J. Structure and stability of solid $\text{Xe}(\text{H}_2)_n$. *J. Chem. Phys.* **142**, 104503 (2015).
33. Bi, T., Zarifi, N., Terpstra, T. & Zurek, E. *Reference Module in Chemistry, Molecular Sciences and Chemical Engineering*. (Elsevier, 2019)
34. Drozdov, A. P., Erements, M. I., Troyan, I. A., Ksenofontov, V. & Shylin, S. I. Conventional superconductivity at 203 kelvin at high pressures in the sulfur hydride system. *Nature* **525**, 73–83 (2015).
35. Bardeen, J., Cooper, L. N. & Schrieffer, J. R. Microscopic theory of superconductivity. *Phys. Rev.* **106**, 162–164 (1957).
36. Drozdov, A. P. & Troyan, M. I. E. Superconductivity above 100 K in PH_3 at high pressures. Preprint at <https://arxiv.org/abs/1508.06224>.
37. Flores-Livas, J. A. et al. Superconductivity in metastable phases of phosphorus-hydride compounds under high pressure. *Phys. Rev. B* **93**, 020508 (2016).
38. Shamp, A. et al. Decomposition products of phosphine under pressure: PH_2 stable and superconducting? *J. Am. Chem. Soc.* **138**, 1884–1892 (2016).
39. Bi, T., Miller, D. P., Shamp, A. & Zurek, E. Superconducting phases of phosphorus hydride under pressure: stabilization by mobile molecular hydrogen. *Angew. Chem. Int. Ed.* **56**, 10192–10195 (2017).
40. Morton, R. J. & Kaiser, R. I. Kinetics of suprathermal hydrogen atom reactions with saturated hydrides in planetary and satellite atmospheres. *Planet. Space Sci.* **51**, 365–373 (2003).
41. Lewis, J. S. *Physics and Chemistry of the Solar System*. in International Geophysics, Vol. 87. (Academic Press, 2004)
42. Fletcher, L., Orton, G., Teanby, N. & Irwin, P. Phosphine on Jupiter and Saturn from Cassini/CIRS. *Icarus* **202**, 543–564 (2009).
43. Pasek, M. A., Mousis, O. & Lunine, J. I. Phosphorus chemistry on Titan. *Icarus* **212**, 751–761 (2011).
44. Mao, H. K. & Bell, P. M. Observations of hydrogen at room temperature (25°C) and high pressure (to 500 Kilobars). *Science* **203**, 1004–1006 (1979).
45. Cotton, F. A., Wilkinson, G., Murillo, C. A. & Bochmann, M. *Advanced inorganic chemistry*, 6th edn. (John Wiley & Sons, 1999).
46. Atkins, P., Overton, T., Rourke, J., Weller, M. & Armstrong, F. *Shriver and Atkins' Inorganic Chemistry*, 5th edn. (W. H. Freeman, 2010).
47. Natta, G. & Casazza, E. La struttura dell'idrogeno fosforato (PH_3) e dell'idrogeno arsenicale (AsH_3). *Gazz. Chim. Ital.* **60**, 851–859 (1930)
48. Stevenson, D. P. The structure of phosphine and related hydrides. *J. Chem. Phys.* **8**, 285–287 (1940).
49. Bondi, A. Van der Waals volumes and radii. *J. Phys. Chem.* **68**, 441–451 (1964).
50. Hardin, A. H. & Harvey, K. B. Infrared absorption of solid phosphine. *Can. J. Chem.* **42**, 84–89 (1964).
51. Francia, M. D. & Nixon, E. R. Infrared study of solid phosphine. *J. Chem. Phys.* **58**, 1061–1065 (1973).
52. Devyatkykh, G. G., Sennikov, P. G. & Nabiev, S. S. Vibrational spectra of volatile inorganic hydrides in the liquid state. *Russ. Chem. Bull.* **48**, 623–639 (1999).
53. Baudler, M. & Glinka, K. Open-chain polyphosphorus hydrides (Phosphines). *Chem. Rev.* **94**, 1273–1297 (1994).
54. Ceppatelli, M., Bini, R. & Schettino, V. High-pressure photodissociation of water as a tool for hydrogen synthesis and fundamental chemistry. *Proc. Natl Acad. Sci. USA* **106**, 11454–11459 (2009).
55. Yuan, Y. et al. Stoichiometric evolutions of PH_3 under high pressure: implication for high- T_c superconducting hydrides. *Natl Sci. Rev.* **6**, 524–531 (2019).
56. Mao, H., Xu, J. & Bell, P. *Pressure-Induced Infrared Spectra of Hydrogen to 542 kbar*. Year book, Vol. 82, 366–372 (Carnegie Institution of Washington, 1983)
57. Binns, J., Dalladay-Simpson, P., Wang, M., Ackland, G. J., Gregoryanz, E. & Howie, R. T. Formation of H_2 -rich iodine-hydrogen compounds at high pressure. *Phys. Rev. B* **97**, 024111 (2018).
58. Pace, E. J. et al. Properties and phase diagram of $(\text{H}_2\text{S})_2\text{H}_2$. *Phys. Rev. B*, **101**, 174511 (2020).
59. Snider, E. et al. Room-temperature superconductivity in a carbonaceous sulfur hydride. *Nature* **586**, 373–377 (2020).
60. Hansen, A. S., Du, L. & Kjaergaard, H. G. Positively charged phosphorus as a hydrogen bond acceptor. *J. Phys. Chem. Lett.* **5**, 4225–4231 (2014).
61. Grabowski, S. J., Alkorta, I. & Elguero, J. Complexes between dihydrogen and amine, phosphine, and arsine derivatives. hydrogen bond versus pnictogen interaction. *J. Phys. Chem. A* **117**, 3243–3251 (2013).
62. Guńka, P. A., Hapka, M., Hanfland, M., Chalaśiński, G. & Zachara, J. Toward heterolytic bond dissociation of dihydrogen: the study of hydrogen in arsenolite under high pressure. *J. Phys. Chem. C* **123**, 16868–16872 (2019).
63. Hoffmann, R. How chemistry and physics meet in the solid state. *Angew. Chem. Int. Ed.* **26**, 846–878 (1987).
64. Liu, M. et al. Unravelling decomposition products of phosphine under high pressure. *J. Raman Spectrosc.* **49**, 721–727 (2018).
65. Greaves, J. S. et al. Phosphine gas in the cloud decks of Venus. *Nat. Astron.* <https://doi.org/10.1038/s41550-020-1174-4> (2020).
66. Lundegaard, L. F., Weck, G., McMahon, M. I., Desgreniers, S. & Loubeyre, P. Observation of an O_8 molecular lattice in the ϵ phase of solid oxygen. *Nature* **443**, 201–204 (2006).
67. Santoro, M. et al. Amorphous silica-like carbon dioxide. *Nature* **441**, 857–860 (2006).
68. Nilges, T., Kersting, M. & Pfeifer, T. A fast low-pressure transport route to large black phosphorus single crystals. *J. Solid State Chem.* **181**, 1707–1711 (2008).
69. Donnerer, C., Scheler, T. & Gregoryanz, E. High-pressure synthesis of noble metal hydrides. *J. Chem. Phys.* **138**, 134507 (2013).
70. Atou, T. & Badding, J. In situ diffraction study of the formation of rhenium hydride at high pressure. *J. Solid State Chem.* **118**, 299–302 (1995).
71. Ceppatelli, M., Gorelli, F. A., Haines, J., Santoro, M. & Bini, R. Probing high-pressure reactions in heterogeneous materials by raman spectroscopy. *Z. Krist. Cryst. Mater.* **229**, 83–91 (2014).

72. Bini, R., Ballerini, R., Pratesi, G. & Jodl, H. J. Experimental setup for Fourier transform infrared spectroscopy studies in condensed matter at high pressure and low temperatures. *Rev. Sci. Instrum.* **68**, 3154–3160 (1997).
73. Bonev, S. A., Schwegler, E., Ogitsu, T. & Galli, G. A quantum fluid of metallic hydrogen suggested by first-principles calculations. *Nature* **431**, 669–672 (2004).
74. Batsanov, S. S. Van der Waals radii of hydrogen in gas-phase and condensed molecules. *Struct. Chem.* **10**, 395–400 (1999).
75. Albright, A. T., Burdett, J. K. & Whangbo, M.-H. *Orbital Interactions in Chemistry, 2nd Edn*, 834 (Wiley, 2013).

Acknowledgements

Thanks are expressed to EC through the European Research Council (ERC) for funding the project PHOSFUN “Phosphorene functionalization: a new platform for advanced multifunctional materials” (Grant Agreement No. 670173) through an ERC Advanced Grant. This study was supported by the Deep Carbon Observatory (DCO) initiative under the project *Physics and Chemistry of Carbon at Extreme Conditions*, by the project “GreenPhos - alta pressione”, by the Italian Ministero dell’Istruzione, dell’Università e della Ricerca (MIUR), by Ente Cassa di Risparmio di Firenze under the project Firenze Hydrolab2.0 and by Fondazione Cassa di Risparmio di Firenze under the project HP-PHOTOCHEM. The authors acknowledge the European Synchrotron Radiation Facility (ESRF) for provision of synchrotron radiation facilities and thank G. Garbarino, M. Mezouar and J. Jacobs for assistance in using beamline ID27. The authors would like to thank Prof. Roberto Righini for useful discussions.

Author contributions

M.C., D.S., and R.B. performed the experiments, analyzed all the data and discussed the results. K.D. analyzed the XRD data and discussed the results. M.S.R. and M.P. discussed the results. M.S.R. synthesized black phosphorus. G.G., J.J., and M.M. assisted at ESRF-ID27. M.C. conceived the experiment and wrote the article.

Competing interests

The authors declare no competing interests.

Additional information

Supplementary information is available for this paper at <https://doi.org/10.1038/s41467-020-19745-2>.

Correspondence and requests for materials should be addressed to M.C.

Peer review information *Nature Communications* thanks the anonymous reviewers for their contribution to the peer review of this work. Peer reviewer reports are available.

Reprints and permission information is available at <http://www.nature.com/reprints>

Publisher’s note Springer Nature remains neutral with regard to jurisdictional claims in published maps and institutional affiliations.



Open Access This article is licensed under a Creative Commons Attribution 4.0 International License, which permits use, sharing, adaptation, distribution and reproduction in any medium or format, as long as you give appropriate credit to the original author(s) and the source, provide a link to the Creative Commons license, and indicate if changes were made. The images or other third party material in this article are included in the article’s Creative Commons license, unless indicated otherwise in a credit line to the material. If material is not included in the article’s Creative Commons license and your intended use is not permitted by statutory regulation or exceeds the permitted use, you will need to obtain permission directly from the copyright holder. To view a copy of this license, visit <http://creativecommons.org/licenses/by/4.0/>.

© The Author(s) 2020